On the interaction of a wind turbine wake with a conventionally neutral atmospheric boundary layer

Amy Hodgkin [a],[*], Georgios Deskos [b], Sylvain Laizet [a]

[a] *Turbulence Simulation Group, Department of Aeronautics, Imperial College London, London, SW7 2AZ, UK*
[b] *National Wind Technology Center, National Renewable Energy Laboratory, Golden, CO, 80401, USA*

ARTICLE INFO

ABSTRACT

In this work, we investigate the dynamics of wind turbine tip-vortex breakdown in a conventionally neutral atmospheric boundary layer (ABL). To this end, high-resolution data are collected from large-eddy simulations of a wind turbine operating within a neutral ABL and studied by means of proper orthogonal decomposition (POD) and Fourier analysis. The high resolution of the generated data in both space and time allows us to gain insight into the tip-vortex breakdown mechanisms by (i) capturing the energy modes of the coherent structures, (ii) studying their contribution to the tip-vortex breakdown through their power spectra functions and mean kinetic energy (MKE) flux, and (iii) analysing the growth rate of each contributing perturbation frequency along tip vortices. Our analysis shows that under a fully turbulent scenario, the growth rate of perturbations along the tip vortices is largest for low wave numbers, i.e. long-wave perturbations. Additionally, the MKE flux reaches its highest value at two diameters downstream of the rotor plane, a behaviour that can be attributed to the coexistence of multiple interacting POD modes, with the streamwise vortex roller mode being the primary contributor to the total MKE flux budget, contributing approximately 24%. Finally, comparisons with a laminar, uniform flow scenario subject to a single-frequency perturbation highlight the differences between the two ambient flow conditions. In the non-turbulent, uniform flow scenario, the growth rate attains its maximum value at a wave number corresponding to the out-of-phase mutual-inductance mechanism, whereas the MKE flux exhibits local minima and maxima along the wake and at different downstream locations depending on the perturbation frequency. Our analyses suggest that the breakdown of the wind turbine tip vortices under a fully turbulent neutral ABL inflow is due to complex interactions across a range of excitation frequencies, in which the mutual-inductance instability may not be the dominant one.

1. Introduction

As governments around the world continue to make commitments for the transition of their economies to carbon neutrality by 2050, wind energy has become a key instrument in achieving their long-term goals. For instance, a recent white paper by the UK government (UK Government, 2020) projects that to achieve net-zero emissions by 2050, the current UK offshore wind capacity must quadruple by 2030, including an additional 40 GW in offshore wind capacity. Similar commitments have been made by the European Union, which envisions the installation of between 400 GW and 450 GW in European waters by 2050 (WindEurope, 2020). To reach such ambitious goals, larger and more efficient wind turbines clustered together in arrays, commonly known as wind farms, need to be designed and deployed. Inherently, in highly dense turbine layouts, individual turbine wakes interfere with the power generation of downstream turbines, thereby limiting the

energy efficiency of the overall farm and costing millions of dollars in losses (Lundquist et al., 2019). Moreover, wake effects can become critically important during the diurnal cycle when a stable atmospheric stratification is created due to the cooling of the ocean surfaclare, which leads to pronounced intra-array and interarray wake effects (Shaw et al., 2022). Such conditions are commonly found in both the North Sea (Platis et al., 2018) and the U.S. East Coast (Pryor et al., 2021), and challenges associated with capturing the interaction of ambient turbulence with wind turbine wakes are well recognised (Veers et al., 2019). To this end, the current work attempts to study the dynamics of the near-wake flow field, and in particular the evolution and fate of the near-wake tip-vortex structures ($x < 3D$, where D is the diameter of a turbine) under a fully developed atmospheric boundary layer (ABL).

Wind turbine tip-vortex stability has been the subject of many previous studies (Widnall, 1972; Gupta and Loewy, 1974; Alfredsson and Dahlberg, 1979; Okulov and Sørensen, 2007; Ivanell et al., 2010;

Sarmast et al., 2014; Sun et al., 2021; Hodgkin et al., 2022b), most of which have considered the tip-vortex stability mechanism under laminar flow conditions and single harmonic perturbations. For instance, Ivanell et al. (2010) and Sarmast et al. (2014) demonstrated the critical role of the mutual-inductance (vortex pairing) instability in the breakdown of a helical tip vortex and the transition to the far-wake field, as well as provided an expression for the "stable" wake length. In a follow-up study, Kleusberg et al. (2019) applied a 10% uniform shear profile and showed that the added shear increases the stable wake length along the top and decreases it along the bottom; they proposed a corrected formula for calculating the length scale based on the original expression of Ivanell et al. (2010). Similarly, Hodgkin et al. (2022b) conducted an extensive analysis of the instability mechanism by considering a large range of shear and thermal stratification strengths. They found that shear has a large impact on the wake length and shape of the wake at the breakdown locations, whereas thermal stratification has only a marginal impact on the wake shape. Hodgkin et al. (2022b) also reported that the instability mechanism depends on the perturbation frequency, rather than the applied inflow conditions. Secondary perturbation frequencies on the tip-vortex system were considered by Santoni et al. (2017) who studied the wake shedding frequency of the turbine tower and nacelle. A study of perturbation frequencies due to blade pitch control actuation was more recently undertaken by Brown et al. (2022), whereas Kleine et al. (2022) considered the impact of the surging frequency of a floating wind turbine on the tip-vortex instability. The study of De Cillis et al. (2022b) used stability analysis to give insight into the origin of coherent structures in the wake. They found that the development of coherent structures is mostly driven by linear mechanisms. This characteristic can be exploited by control strategies to suppress wake meandering and achieve faster wake recovery, further supporting the importance of understanding coherent structures in wind turbine wakes. Additionally, Posa et al. (2021) and Posa and Broglia (2021a,b) conducted extremely high-resolution geometry-resolving simulations of a hydrokinetic turbine with almost two billion mesh nodes to study the tip-vortex instability. They found that short and long wave instabilities result in interaction between neighbouring tip vortices, which leads to momentum recovery farther downstream of the wake. More recently, Posa et al. (2022) and Posa and Broglia (2022) studied the influence an upstream wake on the tip vortices with a large-eddy simulation of two in-line turbines with varying spacing. A key finding of these studies is that the increased turbulence of the upstream wake acts to speed up the tip-vortex instability onset of the downstream wake, but the onset of the instability is almost independent of the spacing between the two turbines.

Under fully turbulent atmospheric conditions, different effects such as shear, veer, and microscale turbulence are synthesised to create a rather complex dynamical input to the tip-vortex system that leads to faster wake recovery (Medici and Alfredsson, 2006; Troldborg et al., 2007; Chamorro and Porté-Agel, 2010). A recent study by De Cillis et al. (2022a) shows that turbulence has a significant impact on the dynamic modes of a wind turbine wake, suggesting that atmospheric turbulence should be accounted for when studying the wake breakdown and its associated mechanisms. In particular, they show that when turbulence is present, the wake coherent structures which originate as tip vortices are lost to modes excited by the ambient turbulence. These turbulent modes are ultimately what cause breakdown of the helical spiral wake. A very recent proper orthogonal decomposition (POD) analysis of a vertical-axis wind turbine by Hellström et al. (2023) also found that changing from uniform inflow to a turbulent boundary layer reduces the relative energy in coherent structures. A thorough analysis of the near wake of a laboratory-scale wind turbine was conducted by Singh et al. (2014). They found that the wake field contains more homogenised scale-dependent velocity increments along with reducing intermittent scales. To this end, a number of models have been proposed based on truncated POD analysis and added stochastic turbulence structures, e.g. Bastine et al. (2014, 2015). These models,

however, were found to overpredict the anisotropy of the wake, as pointed out by Hamilton et al. (2017), who also proposed numerical remedies to address this issue.

Following on previous work in the literature, as well as leveraging existing work within our research group (Hodgkin et al., 2022b,a), we undertake POD analysis of the tip-vortex system under a neutral ABL in order to calculate the mean kinetic energy (MKE) flux of each energy mode. For our analysis we use high-fidelity, turbulence-resolving simulation data. Additional Fourier analysis is carried out to find the growth rate of perturbations in the flow as a function of their wave number. The extracted data and subsequent analysis aim at quantifying the contribution of individual coherent structures (based on their energy content) and their impact on wake recovery. This adds insight into how utility-scale wind turbine tip vortices break down into turbulence and, in turn, drive the far-wake field recovery. The remainder of this paper consists of the methodology in Section 2, followed by the results Section 3 and discussion and conclusions in Section 4.

2. Methodology

The high-fidelity turbulence-resolving simulations in this work are carried out with the wind farm simulator WInc3D (Deskos et al., 2020), which is part of the high-order, finite-difference framework of flow solvers Xcompact3D (Bartholomew et al., 2020). The large-eddy simulations are based on the filtered incompressible Navier-Stokes equation,

$$\frac{\partial u_i}{\partial t} + \frac{1}{2}\left(u_j \frac{\partial u_i}{\partial x_j} + \frac{\partial u_i u_j}{\partial x_j}\right) = -\frac{1}{\rho}\frac{\partial p}{\partial x_i} - \frac{\partial \tau_{ij}}{\partial x_j} + \frac{F_i}{\rho}, \tag{1a}$$

$$\frac{\partial u_i}{\partial x_i} = 0, \tag{1b}$$

where u_i is the velocity vector field, p is the pressure field, ρ is the constant density field, τ_{ij} are the subgrid stresses, F_i accounts for additional forcing (with $i \in \{x, y, z\}$ corresponding to the streamwise, vertical, and spanwise directions, respectively), $Re = U_0 R/\nu$ is the Reynolds number based on the reference freestream velocity (U_0), the turbine radius (R), and the kinematic viscosity (ν). No reference to any filter is explicitly written in the equations; the unknowns u_i, ρ, p should be interpreted as the large-scale filtered component of velocity, density, and pressure. The convective terms are written in the skew-symmetric form, as it allows for the reduction of aliasing errors while remaining energy-conserving (Kravchenko and Moin, 1997).

The governing equations are solved with sixth-order finite-difference schemes on a Cartesian mesh and a fractional-step method with a third-order explicit Adams-Bashforth method for the temporal integration. Within the fractional-step method, the incompressibility condition is dealt with by directly solving a Poisson equation in spectral space using three-dimensional fast Fourier transforms and the concept of the modified wave number. The velocity-pressure mesh arrangement is half staggered to avoid spurious pressure perturbations. More details of the code implementation can be found in Laizet and Lamballais (2009), Laizet and Li (2011), Deskos et al. (2020).

The subgrid stresses, τ_{ij}, are handled explicitly with the Smagorinsky model (Smagorinsky, 1963). The stresses are related to the eddy viscosity, ν_t, expressed as

$$\tau_{ij} = -2\nu_t S_{ij}, \tag{2a}$$

$$\nu_t = (C_s \Delta)^2 |S_{ij}|, \tag{2b}$$

where

$$S_{ij} = \frac{1}{2}\left(\frac{\partial u_i}{\partial x_j} + \frac{\partial u_j}{\partial x_i}\right)$$

is the strain rate tensor, $|S_{ij}| = \sqrt{2S_{ij}S_{ij}}$, Δ is the volumetric grid spacing, and C_s is the Smagorinsky coefficient. The expression

$$C_s = \left(C_0^{n_s} + \left[\kappa\left(\frac{y}{\Delta} + \frac{y_0}{\Delta}\right)^{-n_s}\right]\right)^{-1/n_s}, \tag{3}$$
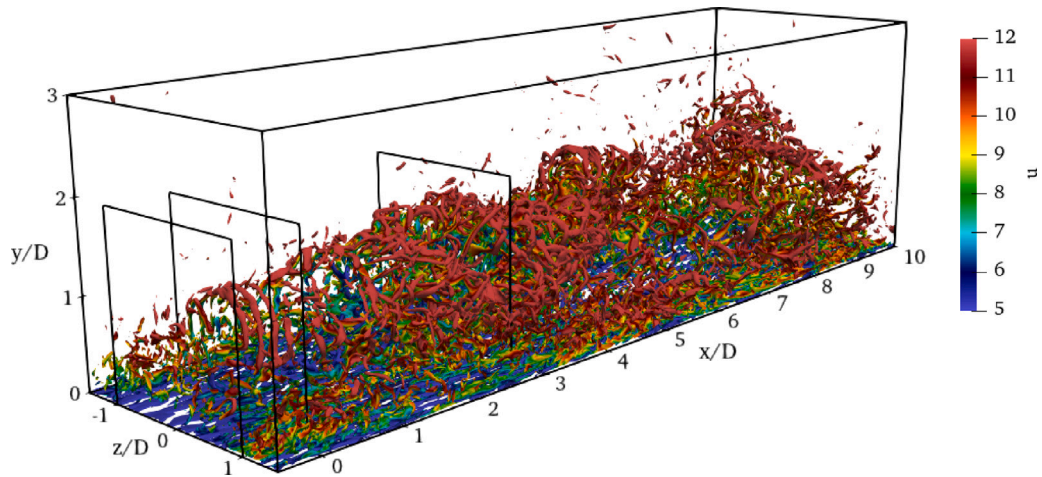
Fig. 1. The saved snapshots for the ABL simulations, showing the location and size of 2D planes for POD analysis at $-0.5D$, $0.25D$, and $3D$. The turbine is located at $(0, y_{hub}, 0)$.

is used to adjust C_s near the wall, to improve log-law mismatch (Mason and Thomson, 1992). κ is the von Kármán constant. Values of $C_0 = 0.14$ and $n_s = 3$ are used in the present setup.

A wall model is applied at the bottom boundary which relates the wall stress to the velocity at the first off-wall grid points using the logarithmic law of the wall (Schumann, 1975),

$$\tau_{i2|w} = -u_*^2 \frac{\tilde{u}_i}{\tilde{u}_r}, \tag{4}$$

where $\tau_{i2|w}$ is the instantaneous local wall stress,

$$u_* = \frac{\tilde{u}_r \kappa}{\ln(y/y_0)}$$

is the friction velocity, y_0 is the surface roughness, and $\tilde{u}_r$ is the local filtered horizontal velocity at the first level, $y = \Delta y/2$. The boundary condition at the bottom wall ($y = 0$) is fixed velocity, with the velocity prescribed by the wall model. The upper y boundary is no-slip. There are periodic boundary conditions in z, and inflow/outflow boundary conditions in x. A precursor simulation must be run to provide the inflow conditions at the x boundary. This is a simulation with the same spatial and temporal discretisation as the secondary simulation, with periodic boundaries in x. It is run until convergence and then inflow planes are collected. The outflow boundary is imposed with one-dimensional convection equations to convect the flow outside the computational domain. The validation of the ABL and wind turbine models, for a slightly different setup due to data availability, can be found in Appendix A.

The NREL 5-MW reference wind turbine (Jonkman et al., 2009), with diameter $D = 126$ m and hub height $y_{hub} = 90$ m, is used for the simulation. The computational domain of $12D \times 8D \times 8D$ is discretised with a uniform mesh of $769 \times 513 \times 512$ nodes. This gives a resolution of 64 nodes per D, which is sufficient to resolve tip vortices in the flow. As a complement to the validation study in Appendix A, the modelled and resolved stresses have been checked to confirm that the majority of the turbulence is being resolved for the spatial resolution considered in the present study. The turbine is placed at midspan, $2D$ downstream of the inlet at $x = 0$. The turbine is run at rated conditions with a tip-speed ratio of $\lambda = \omega_t R/\bar{u}_{hub} = 7$, where ω_t is the angular velocity of the turbine and $\bar{u}_{hub} = 11.4$ m/s. The reference velocity, U_0, is set equal to $\bar{u}_{hub}$. A conventional actuator line method is used to model the turbine via a forcing term added to the momentum equation (Sørensen and Shen, 2002; Deskos et al., 2020). The effects of the tower and nacelle are not included, as the focus of the present study is on the interaction of the rotor dynamics with the ABL. The tower and nacelle would increase the velocity deficit in the wake, with the introduction of additional coherent structures improving the wake recovery (De Cillis

et al., 2021). The full representation of the turbine with tower and nacelle is important for a more realistic configuration, and this will be the focus of a follow-up study.

Snapshots of a reduced domain are saved for postprocessing. The saved domain can be seen in Fig. 1, spanning from $x = -0.5D$ to $x = 10D$. Two-dimensional (2D) y-z planes of the domain are collected for POD analysis (see next section for more detail). The locations of these planes are shown on the figure, spanning $2D$ in the y and z directions.

The profile of the ABL is selected so that the streamwise velocity at hub height is approximately equal to the rated speed of the turbine with a strong shear profile. Based on this, selected parameters are $u_* = 0.67$ m s^{-1} and $y_0 = 0.1$ m. The streamwise velocity profile and turbulence intensity (TI) of the ABL profile can be seen in Fig. 2, with the turbine location shown in dashed lines. There is acceleration of the flow towards the top of the domain, which is expected with large-eddy simulation of the ABL. The log-law is expected to hold up to $y \approx 0.1H$, where H is the boundary layer height (Porté-Agel et al., 2000), but this does not interfere with the key area of interest. The TI at y_{hub} is around 13%.

2.1. Proper orthogonal decomposition

POD is a technique used to detect coherent structures of a flow field by finding orthogonal basis vectors which can be reconstructed to return to the complete flow field (Berkooz et al., 1993). Hence, the flow field can be adequately reconstructed via

$$u_i(x_j, t) = \sum_{k=0}^{N} a_k(t)\psi_k^i(x_j), \tag{5}$$

where the index k corresponds to the kth mode velocity field, ψ_k^i is the velocity of mode k in direction i, and a_k is the corresponding temporal coefficient (amplitude). The modes are ordered in terms of their total energy contribution to the flow with the most dominant mode first. A finite number of modes can be selected to generate a reduced-order model of the flow field. The POD in this study is undertaken using 2D planes of streamwise velocity (see Fig. 1). The simulation is run until statistical convergence is achieved, and then snapshots of the flow field are saved for POD analysis. We note here that based on our convergence study (not shown here), converged statistics can be obtained by saving snapshots every 6 s over a time period of 400 min, for a total of 4000 snapshots. The turbine turns 435° between snapshots, corresponding to about 1.2 rotations.
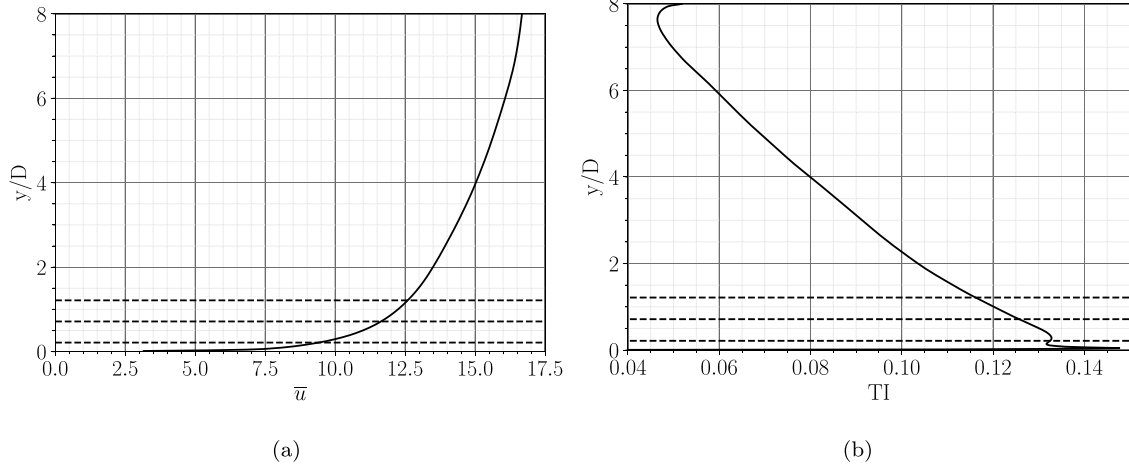
(a)

(b)

Fig. 2. Streamwise velocity and turbulence intensity (TI) profiles of the ABL without turbine. Black dashed lines show the location of the turbine rotor's bottom, hub, and top.

2.2. Mean kinetic energy flux

The MKE flux is used to quantify the impact that coherent structures have on the wake breakdown. A positive MKE flux indicates a contribution to the wake breakdown to turbulence. It corresponds to turbulent energy being brought into the control area from the ambient. A negative MKE flux contributes to delaying the wake breakdown to turbulence. To calculate the MKE flux, the turbulent kinetic energy term is extracted from the transport equation for the MKE,

$$-\frac{\partial}{\partial x_j}\left(\bar{u}_i \overline{u_i' u_j'}\right),\tag{6}$$

with $\overline{u_i' u_j'} = \overline{u_i u_j} - \bar{u}_i \bar{u}_j$ and $\overline{(\cdot)}$ indicates the temporal average. To relate the MKE term to a specific POD mode the following approximation is used:

$$\overline{u_i' u_j'} \approx \overline{\sum_{k=1}^{N}(a_k \psi_k^i)\sum_{l=1}^{N}(a_l \psi_i^l)} =$$

$$\sum_{k=1}^{N}\sum_{l=1}^{N}\overline{a_k a_l}\psi_k^i\psi_j^l = \sum_{k=1}^{N}\lambda_k \psi_k^i\psi_k^j \tag{7}$$

where λ_k is the eigenvalue of mode k, which represents the strength of the kth mode. The MKE flux across two-dimensional cross sections of the flow is calculated. Combining Eqs. (6) and (7) and integrating this term through a circular control surface ($S_c = \pi R_c^2$) enclosed by a line ($L_c = 2\pi R_c$), we may calculate the turbulent MKE flux per unit area for each individual mode k,

$$\mathcal{F}_T^k = \frac{1}{L_c}\int_{S_c} -\frac{\partial}{\partial x_j}\left(\bar{u}_i \lambda_k \psi_i^k \psi_j^k\right) dS_c \,,\tag{8}$$

where $i \in \{x, y, z\}$ and $j \in \{y, z\}$.

2.3. Fourier analysis

A Fourier analysis is used to study the response of excitation frequencies in the wake. The method is inspired by the work of Ivanell et al. (2010) with certain adjustments to allow for a turbulent inflow. The flow field behind the turbine is decomposed into Fourier modes, each corresponding to a frequency in the wake. Fourier modes are calculated from N_F snapshots of the velocity magnitude, $u_{mag} = \sqrt{u_i^2}$,

$$\Phi_n = \frac{1}{N_F}\sum_{m=1}^{N_F} u_{mag,m}e^{-jmn\frac{2\pi}{N_F}},\tag{9}$$

where $j = \sqrt{-1}$, index m corresponds to the mth velocity magnitude field, and index n refers to the nth Fourier mode. A set of 500 snapshots

spaced 0.405 s apart are collected for the Fourier analysis. The time step was selected to capture wave numbers up to $k_p = 6$ (twice the tip-vortex shedding frequency). A different set of snapshots than the POD study but from the same simulation is used because the time step between saved snapshots for POD is too large to capture higher wave numbers, for example those related to the out-of-phase mutual-inductance instability ($k_p = 3/2$ or $k_p = 9/2$). The growth rate of the selected frequency with streamwise location is calculated from the Fourier mode magnitude. This is done by first finding the average of the Fourier mode magnitude in 2D donut-shaped planes that capture the blade tip vortices as a function of x,

$$\langle \Phi_n(x) \rangle = \frac{1}{N_{y,sub}N_{z,sub}}\sum_{y,z}(\|\Phi_n(x,y,z)\|),\tag{10}$$

where $\langle \cdot \rangle$ refers to the spatial average value. The donut region extends between a diameter of $0.7D$ and $1.3D$ to capture the tip vortices while also allowing for some expansion of the wake. Appendix B gives some examples of the Fourier magnitude response in this region. Due to the turbulent noisy flow, the average of the Fourier magnitude is used instead of the maximum of the Fourier magnitude, like in Ivanell et al. (2010). The growth rate of the frequency, σ_n, refers to the section where an exponential growth is observed. It is found from the logarithmic gradient of the average of the mode,

$$\sigma_n = \frac{d\log(\langle \Phi_n \rangle)}{dx}.\tag{11}$$

The linear portion of $\log\langle\Phi_n\rangle$ is found using a gradient search, finding the section of the data in x with the highest regression coefficient.

3. Results

3.1. Instantaneous flow field

Our analysis begins by looking at the wake development in the streamwise direction. Three instantaneous snapshots of vorticity contours, viewed from the top of the domain (x–z plane) are shown in Fig. 3. The magnitude of the vorticity contour was selected to best capture visually the wake features and shape. The vorticity contours are coloured with streamwise velocity, with magnitude increasing with darkness. A white centre line is plotted for reference. The snapshots shown are spaced 100 minutes apart. Distinct features in the wake development can be seen in each snapshot. Vorticity streaks in the ABL along the near wall are visible under the wake structure. The general wake structure is depicted with mostly dark shading, with the lighter contours relating to near-wall vorticity streaks in the boundary layer. The vortical structures in dark navy are high velocity; these exist above the wake deficit region horizontally in line with the turbine. In all
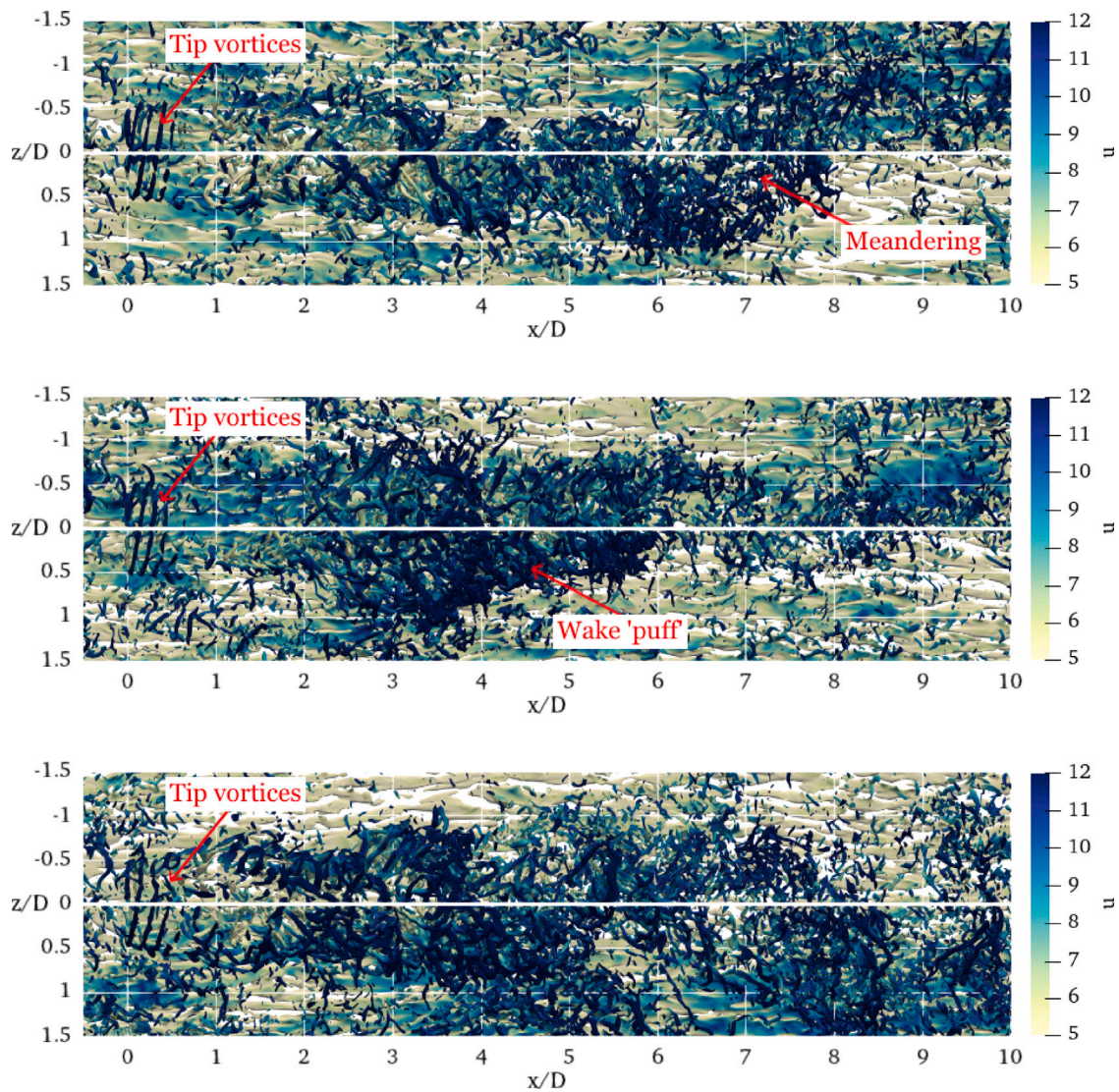
Fig. 3. Plan views of three instantaneous vorticity contours, taken 100 minutes apart, showing the different features present in the fully turbulent wake. A background grid and centreline are plotted in white for reference. Contours are coloured with streamwise velocity, with darker shading representing higher velocity. Some key features of the wake are highlighted with red text. (For interpretation of the references to colour in this figure legend, the reader is referred to the web version of this article.)

snapshots the helical vortices from the blade tips are visible up to $0.5D$ downstream. Approximately three vortex filaments are clearly shown. This structure is disrupted quickly and the wake structure breaks down into multiscale turbulence, which contrasts results in laminar flow. Hodgkin et al. (2022b) show that in the absence of turbulence, the helical vortex continues much farther downstream before breaking down in a regular pattern. After the breakup of the helical spiral, there is a section of lighter shading. Here, the vortical structures are within the wake deficit region downstream of the turbine and thus have lower speed. At $x = 2D$, the vorticity contours become darker because they are situated above the wake deficit, so they have higher velocity. The near wake transitions to the far wake around $1D$–$2D$ (Vermeer et al., 2003), which will be explored in more detail in Section 3.3.

There are large differences in the wake structure farther downstream among the instantaneous snapshots. The flow is highly intermittent, and the wake displays meandering and "puffs" of strong turbulence which move through the domain. In the top plane, wake meandering can be clearly observed. Wake meandering refers to spanwise and vertical displacement of the entire wake from the centreline. Wake meandering is a well-studied feature of wakes that sit in the ABL (Baker and Walker, 1984; Medici and Alfredsson, 2008). The accurate representation of wake meandering in the simulation is important,

as meandering is a key feature of utility-scale wind turbine wakes. It can impact the power output and fatigue of downstream turbines by deflecting the wake into or from downstream turbine paths while also creating unsteady loads. The wake begins roughly parallel to the centreline; however, around $x = 3D$ the wake deflects below the centreline. At $x = 7D$ the wake's deflection changes direction, and it sharply deflects above the centreline. The vertical boundary of the wake also changes with time and downstream location. This is partly shown by the change in shading of the vorticity contours within the wake as they move in and out of the wake's velocity deficit region.

The main feature of the middle figure is a "puff" of strong turbulence above the wake, between $x = 2D$ and $x = 6D$, in the spanwise centre of the domain. Here, the vorticity contours are dark, relating to a high streamwise velocity. The wake between these locations is wider than the wake shown in the top or bottom snapshots. On either side of the "puff" there are vorticity contours of lighter shading which sit within the wake velocity deficit.

The bottom figure shows a roughly straight wake throughout the length of the domain. Here, we note a small bias towards the bottom of the shown domain. Due to the rotational nature of the turbine, there is a preferred direction for meandering (Medici and Alfredsson, 2008). This selection of snapshots gives an example of the different states the wake
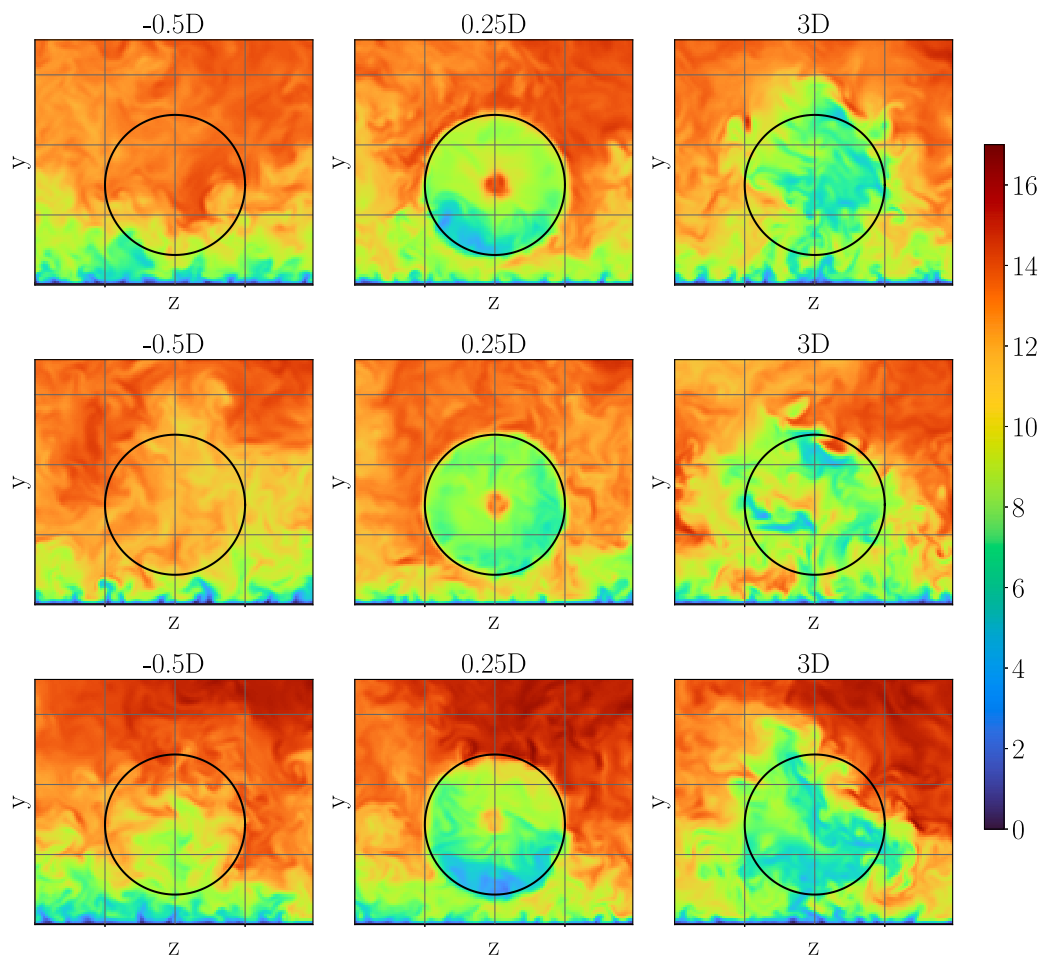
Fig. 4. $y - z$ planes of streamwise velocity at different times at three different downstream locations. The colour map goes from blue to red with increasing velocity. (For interpretation of the references to colour in this figure legend, the reader is referred to the web version of this article.)

can exist in, demonstrating the varied nature and states of the wake as it evolves in time. The complex turbulence in the ABL is disrupting the clean helical spiral tip vortex very early on in the wake development and causing large intermittent structures to move through the domain.

Snapshots of streamwise velocity in the y-z plane at $x = -0.5D$, $0.25D$, and $3D$ are shown in Fig. 4. The magnitude increases from blue to red colouring. The presented locations are examples of flow upstream of the wake, in the near wake and in the far wake. It is important to note that the upstream location will not have exactly the same profile as the freestream ABL profile, as the flow experiences blockage due to the turbine. It can be seen that the wake boundary expands and becomes disrupted as the wake travels downstream. At $-0.5D$, the flow is roughly that of the ABL, there is an increase in velocity when moving away from the wall, and there are velocity fluctuations throughout the domain, giving slightly different profiles at each instantaneous snapshot. At $0.25D$, a velocity deficit can be seen which roughly maps onto the turbine rotor location. This plane is close to the turbine, and the tip vortices are still visible. The tip vortices will act to shield the wake (Lignarolo et al., 2015). At $3D$, the area of velocity deficit centred on the turbine rotor has expanded and the boundary is no longer smooth, unlike at $0.25D$. Velocity fluctuations exist throughout the plane at all locations. These fluctuations do not "see" the turbine location, apart from some small fluctuations localised on the boundary at $0.25D$.

3.2. Power spectra of the wake velocity

Another important aspect of the tip-vortex system breakdown is its turbulence enhancement and the variation of the streamwise velocity

power spectra (PS) function along the wake. Here, we calculate the PS functions using a one-dimensional fast Fourier transform via the Welch method by sampling the streamwise velocity, u, at the hub point, y_{hub}, at three locations, $x = -0.5D$, $0.25D$, and $3D$. Fig. 5 shows the PS functions plotted against the Strouhal number, $St = f D / \bar{u}_{hub}$.

We note that across the three profiles, they all exhibit "plateau" regions at their lower frequencies and approximately for $St < 0.05$ before starting their cascade approximately after $St = 0.1$. Then, the upstream ($x = -0.5D$) and very near-wake field ($x = 0.25D$) follow a decay rate $S_u \propto f^{-5/3}$ similar to three-dimensional isotropic turbulence. In addition, The PS of $x = 0.25D$ appears to only be offset of the $x = -0.5D$, signifying a loss of energy as turbulence enters the turbine wake. This can be attributed to the pressure blockage effect of the turbine rotor as pointed out by Graham (2017). At this point, turbulence at the hub height is only decelerating without distorting. Conversely, as wake mixing at hub height is enhanced, the PS at $x = 3D$ starts to deviate from its upstream counterparts. In particular, the PS is found to follow the $S_u \propto f^{-1/2}$ scaling law, suggesting a much slower decay rate than that of isotropic turbulence in the studied frequency range. This may be attributed to an energy "pumping" mechanism that takes place at $x = 3D$ where MKE is entrained into the wake, enhancing the inertial subrange scales and allowing the larger tip vortices to break down into smaller turbulence structures. This has the effect of increasing the frequency at which the inertial subrange begins. In the following subsection, we will further investigate these mechanisms by examining the PS of the individual POD modes.
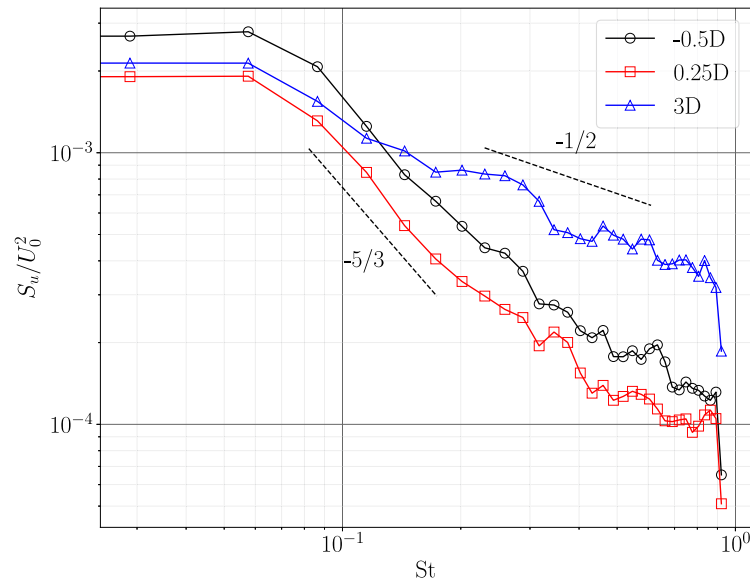
Fig. 5. Power spectra, $S_u(f)$, of the streamwise velocity, u against the Strouhal number, $St = f D/\overline{u}_{hub}$. The spectra are sampled at hub height, y_{hub}, and for one upstream ($x = -0.5D$) and two downstream ($x = 0.25D, 3D$) locations from the turbine rotor plane. The $-5/3$ and $-1/2$ scaling laws are shown with a dashed lines for reference.

3.3. Coherent structures

As we described before, POD is used to extract coherent structures from 2D planes in the flow field. Again, our focus will be on the locations $-0.5D$, $0.25D$, and $3D$. The position and size of these 2D planes are shown in Fig. 1. Other locations are not shown for the sake of saving space but will be included in our discussion. Modes 0 to 7 for $x = -0.5D$, $0.25D$, and $3D$ are shown in Fig. 6, with the location of the turbine rotor represented with a black line. All modes are presented with the same colour map scale, with red representing positive values and blue representing negative values. The arrows represent the tangential velocity. Mode 0 is the mean flow. The POD modes go from larger to smaller scales as the mode number is increased. The mean flow is unipole, whereas mode 1 is a dipole mode, corresponding to a large-scale streamwise vortex roller which is present in the ABL. Quadrupole modes are found at higher mode numbers.

The flow at $-0.5D$ is similar to the ABL flow, with some blockage effects from the turbine. This effect can be seen in mode 0 (mean flow). The mean tangential velocity, represented by the arrows, is not zero as expected in a neutral ABL flow with no Coriolis force. Instead, it is flowing outwards from the turbine centre location. The main structures of the modes are very similar to those at $0.25D$. The primary difference is that at $0.25D$, strong effects near the turbine boundary are seen due to the tip vortices. The distinction between the near wake and far wake can be seen when comparing modes at $0.25D$ and $3D$. The influence of the rotor blades can clearly be seen in modes at $0.25D$ with dark contours around the turbine boundary, whereas modes at $3D$ show less distinction around the turbine boundary and a more general shape which crosses the turbine boundary. When comparing with modes at $-0.5D$, the impact of the turbine on the flow can be seen, for example in the three spots in mode 7. As the wake travels farther downstream than $3D$, the modes keep a similar structure as they expand and become less concentrated. Mode 2 at $3D$ entrains ambient fluid into the wake from the top and rejects it at the sides. The direct influence of the blades is still seen at $1D$, with this impact fading away by two diameters where the transition from near wake to far wake occurs (Vermeer et al., 2003).

When comparing these results with those of Bastine et al. (2014), similar mode shapes are observed. Bastine et al. (2014) preprocess their flow fields to separate the wake dynamics from the ABL dynamics; however, modes show the same trends of moving from larger to smaller scales with largely asymmetric unipole, dipole, and quadrupole modes.

These results are also comparable to other POD analyses of a wind turbine in the ABL. For example, Andersen and Murcia Leon (2022) modelled a row of turbines but highlighted only small differences between first- and last-row turbines. Similarly, Raibaudo et al. (2022), after adding a surge frequency to represent the floating turbine hydrodynamics, reported that their POD analysis using the surge motion had no significant impact on the POD spatial modes.

Fig. 7 shows the normalised eigenvalues in the first 50 modes on a logarithmic scale. The normalised eigenvalue represents the energy content of that mode. The eigenvalues decay with increasing mode number, and this decay slows as mode number increases. There is no significant difference between the results obtained at each downstream location. This suggests that the flow complexity is fairly constant as the wake moves downstream of the turbine. The eigenvalue convergence is slow compared with typical bluff-body flows. The decay trend of the eigenvalues is very similar to that observed by Bastine et al. (2014). Our modes capture slightly less energy per mode than Bastine et al. (2014) until about $k = 30$, when trends converge. The trend is also similar to the eigenvalues reported by Raibaudo et al. (2022).

Fig. 8 shows the PS, S_k, for each mode. The PS is calculated from the temporal coefficients of the POD modes. It gives the frequencies (as Strouhal number) present in each POD mode and their corresponding magnitude. The $-5/3$ scaling is shown with a dashed line for reference. Each POD mode exhibits a full range of frequencies in the captured region with turbulent decay as the Strouhal number increases. The most dominant Strouhal number for each mode is $St \leq 0.05$, which has roughly constant magnitude. The Strouhal number associated with wake meandering is between 0.15 and 0.25 (Medici and Alfredsson, 2008) which is situated in the inertial subrange. In general, the magnitude of S_k gets smaller with the mode number. Mode 0 does not follow the $-5/3$ law, which could be expected, as it is the mean flow with fluctuations removed. On the other hand, modes 1–7 have a fairly good agreement with the $-5/3$ law for all locations. Interestingly, the spectra at $x = -0.5D$ and $0.25D$ are similar, with a noticeable difference only at $3D$. More specifically, at $3D$, the PS function, S_k, exhibits a large offset from the upstream spectra for mode 1. As we discussed previously, mode 1 consists of a large vortex tube/roller (dipole) present in the ABL, which helps to entrain fluid into the rotor area. As a result, it is also one of the most energetic structures which uniformly enhances the spectral content. Modes 2 and 3, on the other hand, show an amplified spectral content towards higher Strouhal number values. Again, the
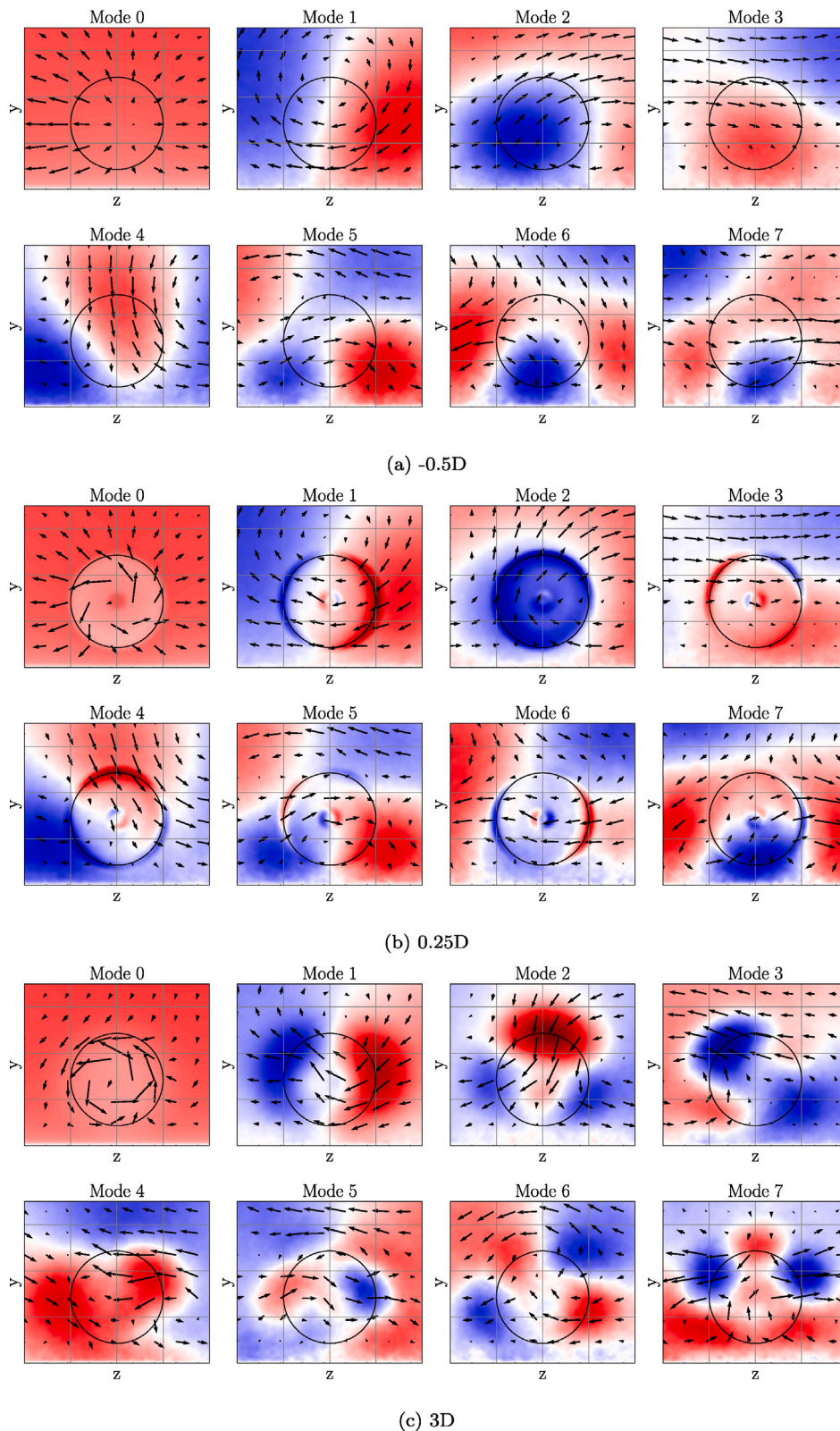
(a) -0.5D

(b) 0.25D

(c) 3D

Fig. 6. Two-dimensional POD modes 0–7 of streamwise velocity. Arrows represent the mode tangential velocity. Mode 0 corresponds to the mean flow.

2D POD mode map at $x = 3D$ suggests (see Fig. 6(c)) that fluid is entrained from atop the wake and escapes from the bottom sides of it. Consequently, larger atmospheric length scales, $l \sim L_{ABL}$, are brought into the wake and mixed with the near-wake turbine scales, $l \sim D$. This allows for a slower decay rate at $x = 3D$. Similar conclusions

can be drawn for the higher modes, i.e. modes 4–7; however, it is worth noting that modes 5 and 7 exhibit a depletion of energy at low Strouhal numbers compared to their counterparts at $x = -0.5D$ and $x = 0.25D$. This behaviour shows that as interactions of the coherent structures become more localised, they tend to contribute less energy
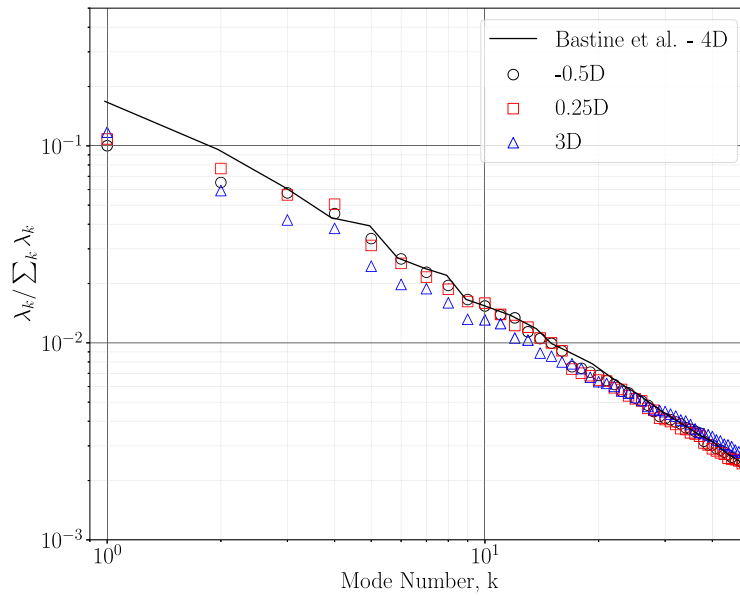
Fig. 7. Normalised eigenvalues for the first 50 modes (not including the mean flow). Reference results from Bastine et al. (2014).
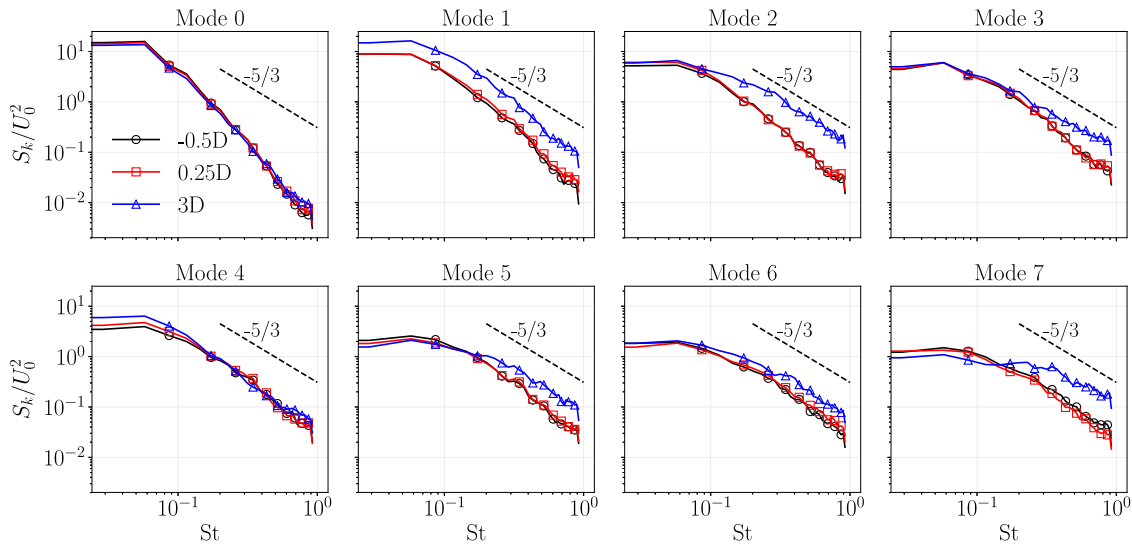

Fig. 8. Power spectra, S_k, for modes 0–7 for three streamwise locations using a logarithmic plot. The dashed line shows the $-5/3$ scaling.

to the larger-scale dynamics of the wake. Finally, we note that these trends between the upstream, $x = -0.5D$, and downstream, $x = 3D$, far wake spectra are consistent with the complete velocity PS taken from a point measurement of the streamwise velocity field at hub height in Fig. 5. The individual mode spectra, however, provide insight into the mechanisms that lead to a slower decay by pointing at the specific modes that contribute to it.

3.4. Mean kinetic energy flux

An MKE flux analysis is used to quantify the contribution of each POD mode to the wake recovery. Comparison will be made with the MKE flux for the complete flow. The complete flow refers to velocity field statistics collected at each time step through the same time period as the collection time of the snapshots. The MKE flux is calculated for 2D planes across a closed circular line of fixed radius, R_c, centred on the turbine (for $R_c = D/2$, this is the black line in Fig. 6). For the complete flow field, the MKE flux can be computed at each streamwise location using all the mesh node in a y-z plane. Fig. 9 shows the complete MKE

flux as a function of streamwise distance along with the MKE flux of POD modes 1–7 for discrete locations.

Upstream of the turbine wake, the MKE flux is always close to zero. At $x = -0.5D$ the complete MKE flux is slightly negative. The MKE fluxes of modes 1 and 2 are positive, whereas the rest of the shown modes have negative MKE flux. The complete MKE flux has an initial local maximum at the hub location ($x = 0$), and then reaches a minimum negative value at $x = 0.0625D$. This initially negative MKE can be explained by the strong tip vortices close to the turbine hub which inhibit mixing. This local minimum was also observed in De Cillis et al. (2021) where the authors used a laminar flow setup. In the ABL case, this negative local minimum is not as strong as for a laminar flow case due to the interaction of the wake with the turbulence from the ABL. The MKE flux for each POD mode gives more insight into this negative local minimum. Modes 5–7 have negative MKE flux. The POD analysis confirms that modes 5–7 have a helical spiral structure. There are six lobes around the turbine boundary; see Hodgkin et al. (2022a) for a reference shape of the helical spiral. These modes are not as dominant as for the laminar flow case, but they contribute to a net-negative MKE flux at this particular location.
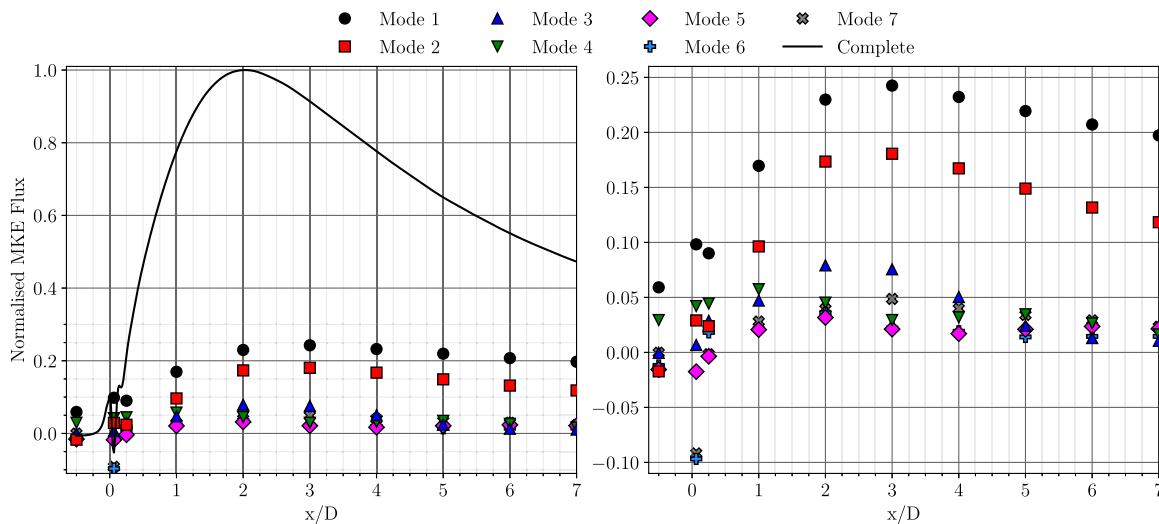
Fig. 9. MKE flux across $1D$ circle, normalised by maximum flux of complete flow field, plotted as a function of streamwise distance, x/D. The black line shows the MKE flux for the complete flow field and symbols show the MKE flux by POD mode. The right figure shows a zoomed-in plot of the mode MKE fluxes.
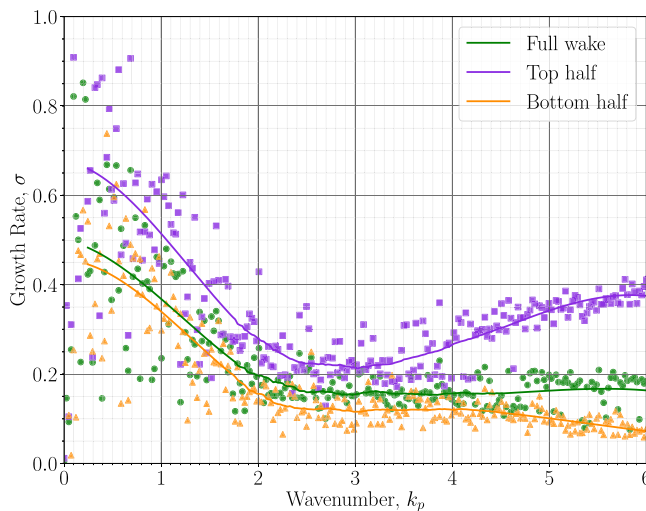

Fig. 10. Growth rate of perturbations in the wake flow against the wavenumber of perturbations.

This local minimum is followed by a steep increase in MKE flux until around $x = 2D$–$3D$. The complete MKE flux analysis shows that the flux of energy into the wake is at its maximum at $x = 2D$. This local peak in MKE flux occurs near the transition from the near-wake field to the far-wake field, where the influence of the rotor blades becomes less important (Vermeer et al., 2003). Interestingly, the local peak for the MKE flux for the dominant modes occurs at $3D$, farther downstream of the MKE peak obtained for the complete flow. This suggests that less energetic modes are contributing the MKE flux around this location and therefore could be important when considering structures that impact the wake breakdown to turbulence. All the POD modes for $x \geq 1D$ have a positive MKE flux. There is only a shielding effect from helical spiral modes with negative MKE flux in the very near wake, for $x < 0.25D$. This contribution comes from modes 5 and up, so they are not the most important in terms of energy content, compared with other POD modes. Finally, it should be noted that modes 1–2 have the largest MKE flux after the MKE peak. Mode 1 reaches a peak of 24%, whereas the combined flux from modes 1–2 corresponds to approximately 40%–45% of the maximum MKE flux from the complete flow.

3.5. Perturbation growth rates

A Fourier analysis can be used to uncover the growth rates for frequencies up to a wavenumber of $k_p = 6$, twice the tip-vortex shedding frequency. Growth rates are calculated for a donut region with diameter between $0.7D$ and $1.3D$ which captures the tip vortices directly downstream of the turbine. Appendix B shows examples of the Fourier response in this region. The area is also split in half horizontally to compare the growth rates between the top and the bottom halves of the wake. Fig. 10 shows the growth rate as a function of wave number, which is the normalised angular frequency, $k_p = \omega/\omega_t$, and ω is the angular frequency of the perturbation in $\mathrm{rad\,s^{-1}}$. The wave number is used as the nondimensional frequency for this part of the study to compare results with literature on growth rates (Ivanell et al., 2010; Kleine et al., 2022). The relationship between Strouhal number and wave number is $k_p = St\,\pi/\lambda \approx St/2$. The phase of the perturbation relates to the phase of oscillations on neighbouring vortex filaments. The wave numbers of out-of-phase perturbations, which relate to the mutual-inductance instability are $k_p = 1.5$ and $k_p = 4.5$, and an in-phase perturbation relates to $k_p = 3$ and $k_p = 6$.

An exponential growth rate was found for all tested wave numbers, although the fit improves as wave numbers increase. Although there is noise in the extracted gradient measurements, a general trend between the growth rates and the wave numbers can be detected. A smooth fit line has been plotted to indicate the trend of the growth rates with wave numbers. The location of exponential growth region generally moves farther downstream as the wave number increases, suggesting the receptive period of the perturbation increases with the wave number. After a period of exponential growth, the value of Fourier magnitude remains roughly constant as the growth rate reduces to zero. The presence of the rotor, which generates perturbations in phase with $k_p = 3$, is clear in the shape of the Fourier magnitude response. It can be seen in Fig. B.15(b) with a large peak in the magnitude at hub location for $k_p = 3$ and $k_p = 6$. The magnitude then quickly reduces before starting its exponential growth region. Wave numbers which are not in phase with the rotor do not exhibit a large peak at the hub location (see Fig. B.15(a) and Fig. B.15(c)).

Across the wake, Fig. 10 shows that the growth rate for low wave numbers begins high and decreases in value until around $k_p = 2.5$. For $k_p > 2.5$, the growth rate increases again in the top half of the wake, and decreases further in the bottom half of the wake. The growth rate remains about constant for the full wake from the sum of the top and bottom halves. The growth rate trend for $k_p < 2.5$ is noisier than for

higher wave numbers where the predicted rates are concentrated on the best-fit line. The growth rates in the top half of the wake are larger than those in the bottom half for the full studied range of wave numbers. This difference remains close to 0.1 for $k_p < 3$ but increases at higher wave numbers where the rates in the top half increase while those in the bottom half decrease slightly. The reduction in growth rate near the bottom could be explained by the presence of the wall, which damps the perturbation growth as well as lowers streamwise velocity due to shear.

Stability theory relates the expected growth rate of a single imposed harmonic perturbation to the phase of the perturbation (Kleine et al., 2022). For a single imposed harmonic perturbation with a wave number of $k_p = pN_b$, the growth rate scales with $\sigma \propto p(1 - p)$, which is a quadratic curve with a maximum value at $p = 1/2$, relating to an out-of-phase perturbation (Kleine et al., 2022). The data in Fig. 10 do not align with the expected trend for the theoretical growth rates, although a minimum growth rate is observed in the top half of the wake for $k_p \approx 3$. This suggests that the effect from each wave number on the wake cannot be superimposed from the theory, and additional mechanisms (other than perturbation phase) impact the growth rates in the turbulent conditions.

The MKE analysis shows that modes 1 and 2, which correspond to a streamwise vortex roller and a mode which entrains fluid into the wake, are responsible for a large portion of the positive MKE flux in the wake. As presented in Fig. 5, there is a turbulent decay as the wave number increases, and the ABL is dominated by low-frequency structures. Based on this, we suggest that these modes entrain ambient fluid into the wake at low frequencies due to the ABL turbulence characteristics. The entrainment of this fluid enhances the growth rate of low-frequency wave numbers in the wake, and more so at the top where the wake interacts with the ambient flow. It should be noted that the growth rate at $k_p = 0$ is zero but jumps to a large value for small increases in wave number.

The wave number range presented in Fig. 10 relates mostly to long-wave perturbations, which are long compared with the size of the vortex core and in an ideal case contribute to the oscillations of the entire vortex filaments, leading to vortex pairing. As the wave number increases towards the end of the studied range, the perturbations tend towards short-wave perturbations, which are closer in size to the vortex core, and internally perturb the vortex core, breaking up the coherent vortex filaments into smaller-scale structures. The combined effect of perturbations with these length scales leads to the rapid breakdown of the wake (Leweke et al., 2014). Fig. 10 shows that the growth rates of the perturbations increases in the top half of the wake as the wave numbers tend towards short-wave instabilities. We suggest that the effect of short-wave instabilities on wake breakdown is important due to their action in breaking up the vortex filament into smaller scales. This effect may be especially important in turbulent flow because the coherent vortex filaments are dispersed early, making the vortex pairing mechanism obsolete. Finally, we note that due to the increased receptive period, growth at higher wave numbers occurs farther downstream where the TI is higher. This could either be contributing to the increased growth rates in the top half or it could be an indication that initially dominant long-wave instabilities are overtaken by dominant short-wave instabilities as the wake evolves downstream.

Finally, we hypothesise that the growth rates in the ABL do not obey the theoretical one due to the quick decay of the helical tip-vortex structure by $x = 0.5D$ (see Fig. 3). As a result, the relative meaning of *in-phase* and *out-of-phase* perturbations is lost. Therefore, the growth rate does not follow the expected relationship with wave number, which is predicted based on the perturbation phase. Instead, the change in growth rate with wave number can be attributed to other factors, such as the turbulence properties in the ambient flow, effects from the ground, and the dynamics of short-wave instabilities. The present analysis suggests that the mutual-inductance instability is not the dominant mechanism that leads to the recovery of the main body of the wake.

3.6. Comparison between fully turbulent and laminar inflow conditions

In this part of the manuscript, the POD, MKE, and Fourier results are compared with the data obtained by the authors for a turbine immersed in a laminar flow (Hodgkin et al., 2022b,a). These previous studies looked at the influence of shear and thermal stratification on the evolution of the tip vortices when subject to a single harmonic tip perturbation to trigger wake breakdown via the mutual-inductance instability. In a uniform flow, the wake's helical spiral can be observed far downstream of the turbine, and vortex pairing can be observed between $x = 1D$ and $1.5D$, depending on the perturbation wave number. The influence of the perturbation can be seen up to $4D$ downstream of the turbine (Hodgkin et al., 2022b,a). In the present ABL case, as shown in Fig. 3, the helical vortex breaks down at around $x = 0.5D$, and the vortex filaments are quickly dispersed.

There are significant differences between the POD modes obtained with a laminar flow and with an ABL, both in terms of shape and energy content. In the study of Hodgkin et al. (2022a), four main modes (or two pairs of modes) were observed, making up for at least 80% of the total energy for all studied setups. These four modes relate to the helical spiral tip vortex and the applied harmonic perturbation (or mutual-inductance instability). In comparison, the current ABL setup requires 257, 243, and 305 modes to capture at least 80% of the energy at $-0.5D$, $0.25D$, and $3D$, respectively. In the ABL case, modes that display the helical tip vortex are only observed very close to the turbine ($x < 0.1D$), e.g. modes 5–7. The interaction of the wake's helical spiral tip vortex with the ABL contrasts with the rather clean dynamics observed in the laminar flow case and instead requires a large number of POD modes to be captured properly.

To further understand the impact that the coherent structures from the ABL have on the turbine wake breakdown, the MKE flux in the near wake can be compared for the laminar case and the ABL case. Fig. 11 shows a comparison of the MKE flux for the ABL case and for two uniform flow cases with harmonic tip perturbations with wave numbers of $3/2$ and $9/2$, normalised by the reference streamwise velocity cubed. This figure highlights the important role that coherent structures from the ABL have on the MKE flux. For a control radius $R_c = R$, shown in Fig. 11(a), both curves exhibit a local minimum at the same streamwise location due to strong tip vortices which inhibit mixing. The magnitude of this local minimum is far larger for the uniform flow. This highlights how much stronger the shielding effect of the tip vortices is in a uniform flow. The MKE flux in the uniform flow case then remains roughly very small through the rest of the near wake, while it is growing positively for the ABL case, suggesting more transfer of energy between the turbine wake and the ABL. Basically, the ABL is energising the turbine wake. For the uniform flow case, the mutual-inductance instability caused by the tip perturbation is the dominant instability of the tip vortices. This instability acts on the wake boundary, which expands as it moves downstream. Due to this expansion, the influence of the mutual-inductance instability cannot really be seen with $R_c = R$.

Fig. 11(b) shows the MKE flux evolution for a larger control area with $R_c = 1.2R$. A strong influence of the tip perturbation wave number can be observed for the uniform flow cases, with strong negative/positive oscillations for the MKE flux, especially for $k_p = 9/2$, a positive local maximum at $x = D$, and a negative local minimum at $x = 1.25D$. For the wave number $k_p = 3/2$, the local negative minimum has a low amplitude while the local positive maximum has a large amplitude, much higher than the amplitude of the MKE flux for the ABL case. In contrast to the uniform flow case, the MKE flux for the ABL case with $R_c = 1.2R$ shows a similar trend to the MKE flux with $R_c = R$, with a gradual positive increase of MKE flux. We note that the MKE flux for the ABL case is much smoother than the one observed for the uniform flow case. In the ABL case, there are many superposed frequencies which make up the turbulence of the flow field. This means that there is a full range of interacting instabilities from very low frequency to high frequency, rather than one main instability mechanism driving
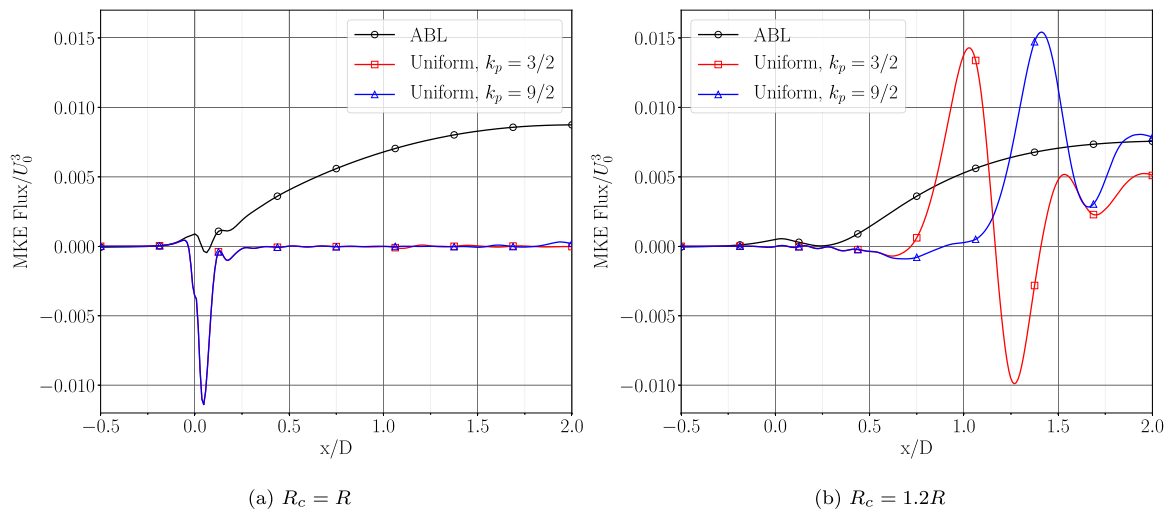
Fig. 11. Near-wake MKE flux for ABL and uniform flow with harmonic tip perturbation with wave number (k_p) equal to 3/2 and 9/2, normalised by U_0^3, plotted as a function of streamwise location, x/D.

the recovery of the wake (i.e. the mutual-inductance instability). The ABL turbulence interacts with the wake dynamics to generate coherent structures (POD modes) that disrupt the wake and bring turbulent energy into the wake to break it up. These conclusions are consistent with the findings of De Cillis et al. (2022a).

The Fourier analysis shows that the growth rates of perturbations in an ABL do not follow the theoretical solution, and the phase of the perturbation does not seem to have a strong influence in the growth rate trend. Instead, high growth rates are seen for long-wave and short-wave perturbations. This result differs significantly from uniform flow results and suggests that the mutual-inductance instability can not be considered the dominant instability of a wake in a turbulent ABL. We note that the combination of long-wave instabilities and short-wave instabilities is complex (Leweke et al., 2014) and still not fully understood. Additionally, for the laminar case, shear acts to increase the growth rate at the bottom and decrease the growth rate at the top due to a reduced helix pitch at the bottom, which encourages vortex pairing (Hodgkin et al., 2022b). This trend was not observed for the ABL and reduced growth rates at the bottom half of the wake. This could be due to damping effects from the ground. Another explanation is that the effect of shear on perturbation growth, where vortex pairing is not the main instability mechanism, has an opposite effect on perturbation growth rates due to reduced velocities. We suggest that in the ABL case, factors other than phase are the primary drivers of the perturbation growth rates, such as the ABL turbulence statistics, ground damping effects, and the dynamics of short-wave instabilities which break up coherent vortex filaments.

4. Discussion and conclusions

In this work, we conducted POD analysis of a turbine wake in a conventionally neutral ABL with the purpose of improving our understanding of the mechanisms triggering the tip-vortex breakdown in the near-wake field. The study is done by analysing results from a high-resolution large-eddy simulation of a single turbine immersed in the atmospheric turbulence. The analysis includes visualisations of the instantaneous snapshots of the flow field, POD, and MKE flux calculations and a Fourier analysis. The MKE calculations in particular, provide insight into the contribution of coherent structures to the wake recovery while the Fourier analysis finds the growth rate of excitation perturbations in the wake. For completeness, comparisons are also made with a wake generated by a turbine immersed in laminar flow.

In the turbulent boundary layer, the helical tip-vortex structure from the turbine blades is visible in the first $0.5D$ downstream of the turbine. This vortex is disrupted quickly and breaks down into multiscale turbulence. The rest of the wake behind the turbine is made up of highly turbulent, high-speed, vortical structures. The location of the wake boundary varies in time. The flow in the wake is highly intermittent, with meandering features and "puffs" of turbulence which are being convected as the wake evolves downstream of the turbines. The wake boundary expands horizontally and vertically as it moves downstream, and vortical structures in the wake oscillate in and out of the wake deficit. The PS at hub height first follows the classic $-5/3$ scaling (typical of homogeneous isotropic turbulence) for $x = -0.5D$ and $0.25D$. In the far wake from $3D$, the PS decays more slowly and follows a $-1/2$ scaling for the studied frequency range. This could be explained by increased turbulence levels in the far wake as a result of a transfer of coherent structures from the boundary layer to the turbine wake.

The POD analysis shows modes which decrease in scale with increasing mode number. The direct influence of the turbine rotor is clearly observed for $0.25D$ but then is reduced after $3D$ downstream of the turbine, although the shape of the modes is similar. The observed decay for the eigenvalues of the modes as a function of mode number is similar to trends observed in the literature (Bastine et al., 2014). The PS of the POD modes show that modes 1–7 mostly follow a conventional $-5/3$ scaling. The PS at $-0.5D$ and $0.25D$ have similar shape, whereas a slower decay is reported farther downstream of the turbine. A few hundred modes are needed to reconstruct 80% of the energy for the wake immersed in a turbulent boundary layer, in contrast to only four POD modes for the wake immersed in a laminar flow.

The MKE flux for the complete flow field is maximal at $2D$ downstream of the turbine, aligning roughly with the transition from near wake to far wake. However the two most dominant modes have their maximum MKE flux at $3D$, with mode 1 contributing 24% of the complete flow maximum MKE flux at this location. Very close to the turbine, at $0.0625D$, there is a negative minimum in the complete flow MKE flux. This is due to negative MKE flux in modes 5–7, which all relate to tip-vortex structures. These POD modes are far less important in the turbulent boundary layer case than in the laminar case. For $x \geq 1D$, the MKE flux of modes 1–7 is positive, and the highest MKE flux occurs for modes 1–2. These results shows that in the turbulent boundary layer case, coherent turbulent structures from the boundary layer are energising the turbine wake; this phenomenon is possibly one of the main driving factors of the wake breakdown to turbulence.

A Fourier analysis is used to calculate the growth rate of different wave numbers in the wake. There is a region of exponential growth behind the turbine for each wave number. The analysis shows that the growth rates do not follow the theoretical solution that predicts growth rate based on the perturbation phase. There is instead a decrease in growth rate until about $k_p = 2.5$, where the growth rates in the bottom half reduce further while in the top half they increase again until the end of the studied range ($k_p = 6$). This suggests that perturbation phase is not the main driver of the growth rates, unlike in laminar flow setups, and therefore the mutual-inductance instability is not the main instability causing wake breakdown in the ABL case. This could be due to the helical spiral vortex structure being disturbed early in the wake, which negates the definitions of in-phase and out-of-phase perturbations. Additionally, the growth rates in the bottom half of the wake are smaller than for the top half, an opposite trend when compared to results in uniform shear where the perturbations at the bottom of the wake grow faster due to a reduced helix pitch. We suggest that the trends for the growth rate could be attributed to the ABL turbulence statistics, ground damping effects, and the presence of short-wave instabilities. Further investigations into these factors may provide useful insight into wake breakdown in a turbulent ABL.

To summarise, findings from the range of analyses of a wake in a neutral ABL indicate that the breakdown mechanisms of a wake in a turbulent environment are very different to those in a laminar environment. Importantly, there is a full range of instabilities from very low frequency to high frequencies whose effects on the vortex structures are combined, with a strong effect on the development of the wake downstream of the turbines. Unlike the laminar inflow, where perturbation phase remains very important to the tip-vortex breakdown mechanisms, factors such as the ambient turbulence, ground damping, and complex interaction of short-wave and long-wave instabilities on the vortex core may be relevant in a better understanding of the interaction of a wind turbine wake with a conventionally neutral ABL.

Future work will look at wake-to-wake interaction by studying two in-line turbines immersed in a turbulent boundary layer. We will also look at the influence of the tower and nacelle and how their wake can influence the breakdown to turbulence for the tip vortices.

CRediT authorship contribution statement

Amy Hodgkin: Conceptualization, Methodology, Validation, Formal analysis, Investigation, Writing – original draft, Writing – review & editing, Visualization. **Georgios Deskos:** Conceptualization, Software, Investigation, Writing – original draft, Writing – review & editing. **Sylvain Laizet:** Conceptualization, Software, Writing – review & editing, Supervision, Funding acquisition.

Declaration of competing interest

The authors declare that they have no known competing financial interests or personal relationships that could have appeared to influence the work reported in this paper.

Data availability

Data will be made available on request.

Acknowledgements

Appendix A. Validation

WInc3D has been validated for the simulation of an ABL, combined with the use of an actuator line method to model the blades of an immersed turbines in the ABL. Reference experimental (Chamorro and Porté-Agel, 2010) and numerical (Stevens et al., 2018) data are used for this appendix for comparison. The experimental data relate to a laboratory-scale boundary layer for which the values of streamwise velocity and TI which will be used for comparison. For this setup, $z_0 = 0.00003$ m and $u_* = 0.102$ m/s. The computational domain is 4.32 m $\times$ 0.46 m $\times$ 0.72 m discretised with $289 \times 65 \times 48$ mesh nodes. The turbine has a diameter of 0.15 m and a hub height of 0.125 m. The blades modelled are GWS/EP-6030. The turbine operates with a tip speed ratio of 4, based on a hub height velocity of 2.1 m/s. The tower and nacelle are not included in the validation. Note that the validation case setup differs slightly from the setup of the main case of this study in order to exactly match the available reference data.

The mean streamwise velocity profiles, shown in Fig. A.12, are in good agreement with the reference experimental and the numerical ones. The TI profiles, in Fig. A.13, have a similar level of agreement with the reference experimental results at $2D$ and $3D$ downstream of the turbine; only small differences at the hub height are reported close to the turbine (as the nacelle is not included in the present simulation). Overall the present data are similar to the reference numerical data for all locations. The agreement between the two sets of numerical data becomes stronger farther downstream of the turbine rotor, for $x = 5D$ downstream of the turbine and beyond. The ability to correctly predict the wake behaviour at these locations is important for wind farm modelling, as the streamwise spacing between turbines is typically around $5D$ to $7D$ in modern wind farms.

The resolved and modelled stresses (τ) normalised by u_*^2 of the precursor ABL simulation (without turbine) are presented in Fig. A.14 to confirm the ability of WInc3D to resolve the majority of the turbulent stresses (Deskos, 2018) for the spatial resolution under consideration. The figure shows that the computational setup of WInc3D is adequate for resolving the majority of the turbulent stresses and only very near the wall are the majority of stresses modelled. Overall, it can be concluded that WInc3D is able to capture the main features of the wake generated by a turbine immersed in an ABL.

Appendix B. Growth rate calculations

The growth rates are calculated from the average of the Fourier magnitude in a "donut-shaped" region with radius between $0.7R$ and $1.3R$, which captures the tip vortices. The magnitude of the Fourier modes for $k_p = 1.5$, $k_p = 3$ and $k_p = 4.5$ are presented in this appendix to show what the growth of in-phase and out-of-phase perturbations looks like, as well as to give a visual representation of the area over which the Fourier mode is averaged. Fig. B.15 shows the Fourier magnitude in the donut region over which the average is taken at $-0.5D$, $0D$, $0.25D$, and
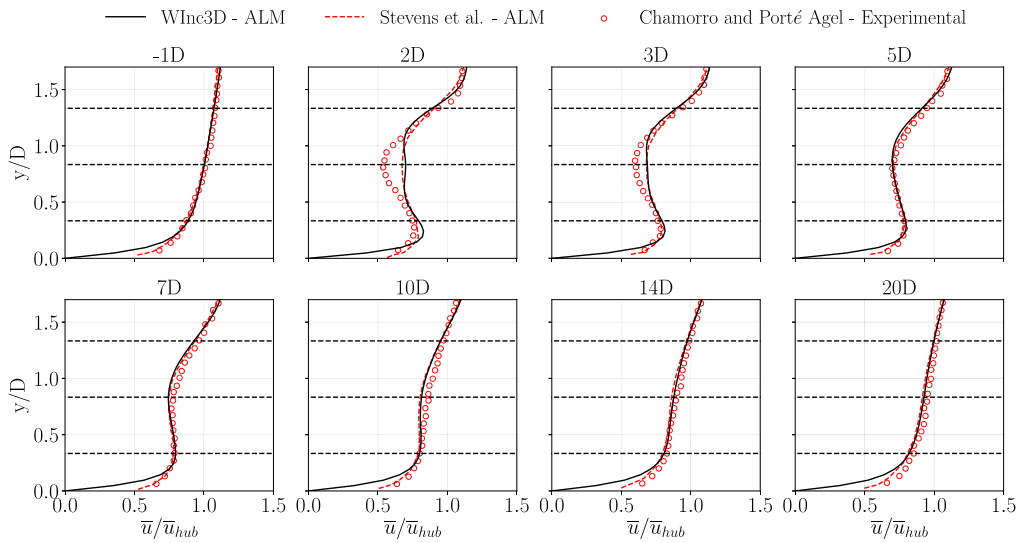
Fig. A.12. Mean streamwise velocity profiles of the validation case with a turbine at multiple downstream locations. Red line shows the results by Stevens et al. (2018) with an actuator line method. Red circles show the experimental results of Chamorro and Porté-Agel (2010). Black lines show the results obtained with WInc3D. Black dashed lines show the location of turbine rotor's bottom, hub and top.
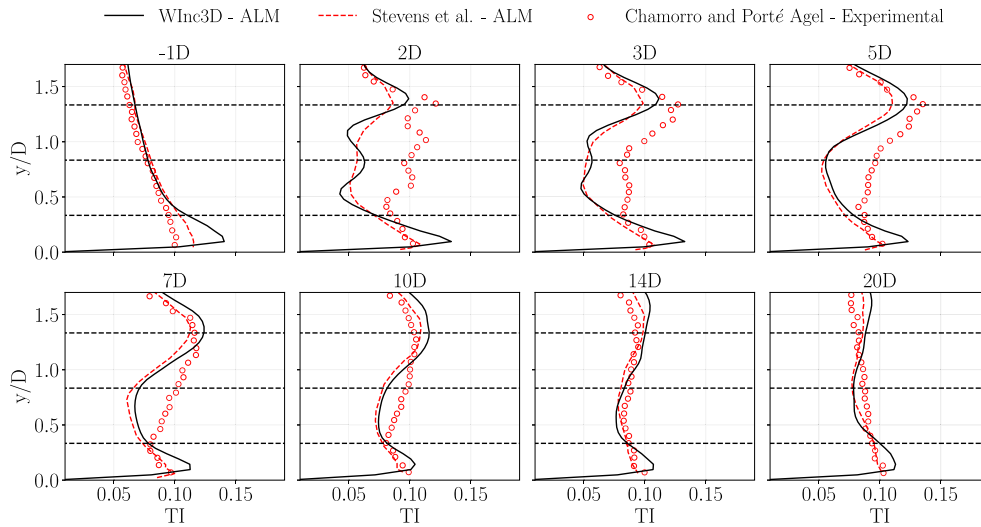

Fig. A.13. Streamwise turbulence intensity (TI) of the validation case with a turbine at multiple downstream locations. Red line shows the results by Stevens et al. (2018) with an actuator line method. Red circles show the experimental results of Chamorro and Porté-Agel (2010). Black lines show the results obtained with WInc3D. Black dashed lines show the location of turbine rotor's bottom, hub and top.
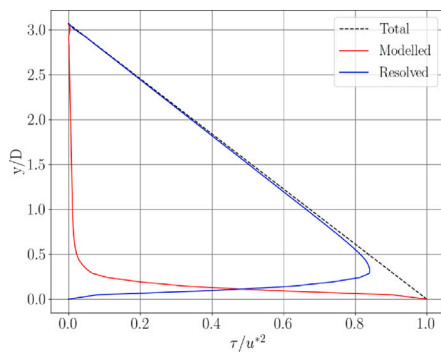

Fig. A.14. Resolved and modelled stresses, normalised by u_*^2 for the ABL (without turbine) of the validation case. Total stresses should follow a straight line with gradient of −1.

$3D$. A clear difference between in-phase and out-of-phase perturbations is shown at and near the rotor location. The influence of the blade tips (which are in phase with $k_p = 3$) is seen in Fig. B.15(b). This influence is no longer present at $3D$ downstream, where the magnitude profile is comparable with the other figures. The response at $k_p = 1.5$ and $k_p = 4.5$, in Fig. B.15(a) and B.15(c), show no imprint of the rotor, as expected, and instead the perturbations are reduced on entry to the turbine and then grow again within the wake. Unlike in a laminar flow case, wavelengths which correspond to the selected wave number cannot be observed, and instead the Fourier response is dominated with small-scale fluctuations. This supports the suggestion that short-wave (high-frequency) perturbations are important in the turbulent ABL wake, as their contribution to breaking up coherent vortex filaments is clearly observed in the appearance of the Fourier magnitude response.
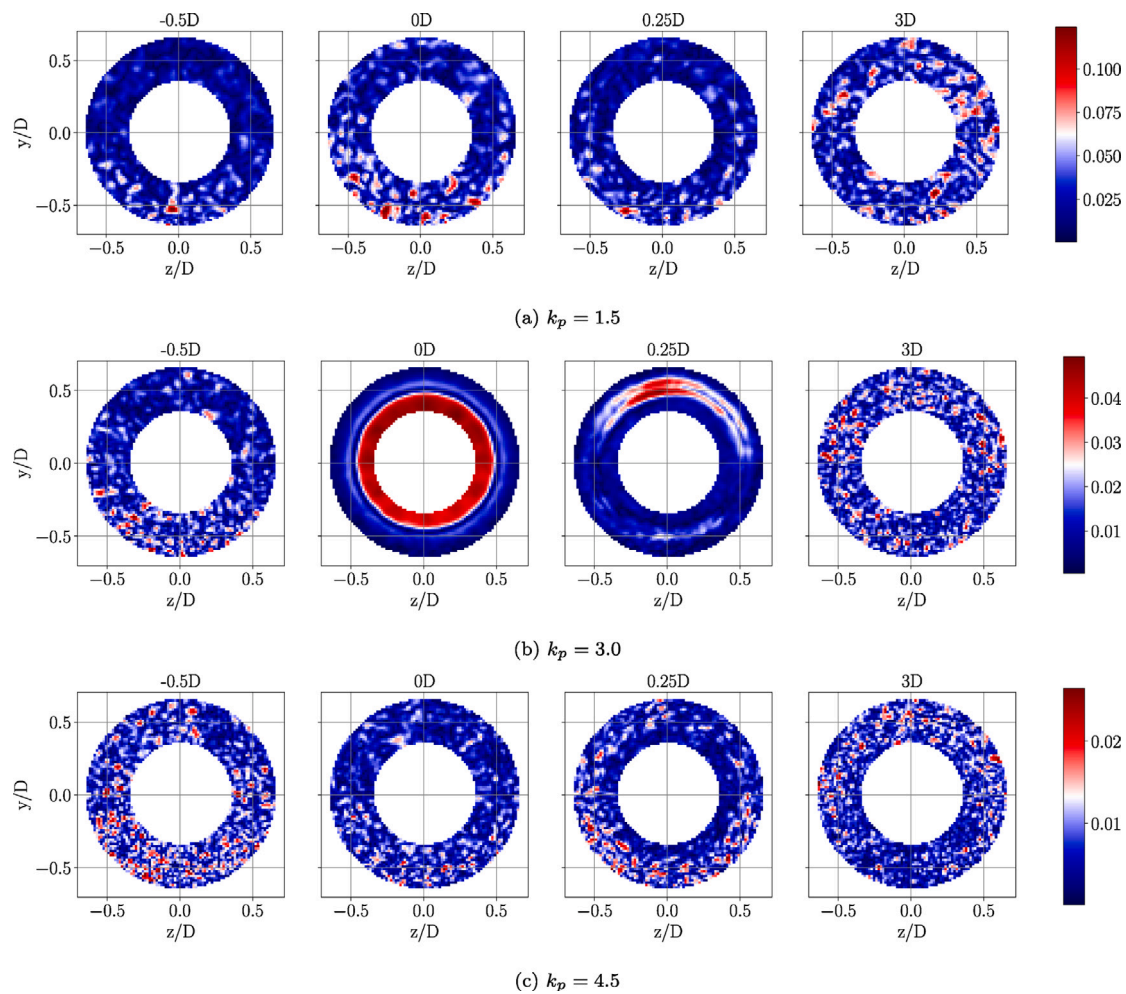
(a) $k_p = 1.5$

(b) $k_p = 3.0$

(c) $k_p = 4.5$

Fig. B.15. Magnitude of the Fourier mode for three wave numbers. The average value used to find the growth rate is calculated for the donut-shaped region shown between $0.7D$ and $1.3D$, which captures the tip vortices. Wave numbers are correct to 2 significant figures.

References

Alfredsson, P., Dahlberg, J., 1979. A Preliminary Wind Tunnel Study of Windmill Wake Dispersion in Various Flow Conditions.

Andersen, S.J., Murcia Leon, J.P., 2022. Predictive and stochastic reduced-order modeling of wind turbine wake dynamics. Wind Energy Sci. 7 (5), 2117–2133.

Baker, R.W., Walker, S.N., 1984. Wake measurements behind a large horizontal axis wind turbine generator. Sol. Energy 33 (1), 5–12.

Bartholomew, P., Deskos, G., Frantz, R., Schuch, F.N., Lamballais, E., Laizet, S., 2020. Xcompact3D: An open-source framework for solving turbulence problems on a Cartesian mesh. SoftwareX 12, 100550.

Bastine, D., Witha, B., Wächter, M., Peinke, J., 2014. POD analysis of a wind turbine wake in a turbulent atmospheric boundary layer. J. Phys.: Conf. Ser. 524 (1), 012153.

Bastine, D., Witha, B., Wächter, M., Peinke, J., 2015. Towards a simplified dynamic wake model using POD analysis. Energies 8 (2), 895–920.

Berkooz, G., Holmes, P., Lumley, J.L., 1993. The proper orthogonal decomposition in the analysis of turbulent flows. Annu. Rev. Fluid Mech. 25 (1), 539–575.

Brown, K., Houck, D., Maniaci, D., Westergaard, C., Kelley, C., 2022. Accelerated wind-turbine wake recovery through actuation of the tip-vortex instability. AIAA J. 60 (5), 3298–3310.

Chamorro, L.P., Porté-Agel, F., 2010. Effects of thermal stability and incoming boundary-layer flow characteristics on wind-turbine wakes: A wind-tunnel study. Bound.-Lay. Meteorol. 136 (3), 515–533.

De Cillis, G., Cherubini, S., Semeraro, O., Leonardi, S., De Palma, P., 2021. POD-based analysis of a wind turbine wake under the influence of tower and nacelle. Wind Energy 24 (6), 609–633.

De Cillis, G., Cherubini, S., Semeraro, O., Leonardi, S., De Palma, P., 2022a. The influence of incoming turbulence on the dynamic modes of an NREL-5MW wind turbine wake. Renew. Energy 183, 601–616.

De Cillis, G., Cherubini, S., Semeraro, O., Leonardi, S., De Palma, P., 2022b. Stability and optimal forcing analysis of a wind turbine wake: Comparison with POD. Renew. Energy 181, 765–785.

Deskos, G., 2018. Numerical Simulations of Wind Turbine Wakes (Ph.D. thesis). Imperial College, London.

Deskos, G., Laizet, S., Palacios, R., 2020. WInc3D: A novel framework for turbulence-resolving simulations of wind farm wake interactions. Wind Energy 23 (3), 779–794.

Graham, J.M.R., 2017. Rapid distortion of turbulence into an open turbine rotor. J. Fluid Mech. 825, 764–794.

Gupta, B.P., Loewy, R.G., 1974. Theoretical analysis of the aerodynamic stability of multiple, interdigitated helical vortices. AIAA J. 12 (10), 1381–1387.

Hamilton, N., Tutkun, M., Cal, R.B., 2017. Anisotropic character of low-order turbulent flow descriptions through the proper orthogonal decomposition. Phys. Rev. Fluids 2 (1), 014601.

Hellström, L., Hohman, T., Smits, A., 2023. POD analysis of the structure of vertical axis wind turbine wakes. J. Wind Eng. Ind. Aerodyn. 237, 105403.

Hodgkin, A., Laizet, S., Deskos, G., 2022a. Do ambient shear and thermal stratification impact wind turbine tip-vortex breakdown? J. Phys.: Conf. Ser. 2265 (2), 022061.

Hodgkin, A., Laizet, S., Deskos, G., 2022b. Numerical investigation of the influence of shear and thermal stratification on the wind turbine tip-vortex stability. Wind Energy 25 (7), 1270–1289.

Ivanell, S., Mikkelsen, R., Sørensen, J.N., Henningson, D., 2010. Stability analysis of the tip vortices of a wind turbine. Wind Energy 13 (8), 705–715.

Jonkman, J., Butterfield, S., Musial, W., Scott, G., 2009. Definition of a 5-MW Reference Wind Turbine for Offshore System Development. Technical Report, National Renewable Energy Lab.(NREL), Golden, CO (United States).

Kleine, V.G., Franceschini, L., Carmo, B.S., Hanifi, A., Henningson, D.S., 2022. The stability of wakes of floating wind turbines. Phys. Fluids 34 (7), 074106.

Kleusberg, E., Benard, S., Henningson, D., 2019. Tip-vortex breakdown of wind turbines subject to shear. Wind Energy 22 (12), 1789–1799.

Kravchenko, A., Moin, P., 1997. On the effect of numerical errors in large eddy simulations of turbulent flows. J. Comput. Phys. 131 (2), 310–322.

Laizet, S., Lamballais, E., 2009. High-order compact schemes for incompressible flows : A simple and efficient method with quasi-spectral accuracy. J. Comput. Phys. 228 (16), 5989–6015.

Laizet, S., Li, N., 2011. Incompact3d : A powerful tool to tackle turbulence problems with up to O (10 5) computational cores. Internat. J. Numer. Methods Fluids 67, 1735–1757.

Leweke, T., Quaranta, H.U., Bolnot, H., Blanco-Rodríguez, F.J., Le Dizès, S., 2014. Long-and short-wave instabilities in helical vortices. J. Phys.: Conf. Ser. 524 (1), 012154.

Lignarolo, L.E.M., Ragni, D., Scarano, F., Ferreira, C.S., Van Bussel, G.J.W., 2015. Tip-vortex instability and turbulent mixing in wind-turbine wakes. J. Fluid Mech. 781, 467–493.

Lundquist, J., DuVivier, K., Kaffine, D., Tomaszewski, J., 2019. Costs and consequences of wind turbine wake effects arising from uncoordinated wind energy development. Nature Energy 4 (1), 26–34.

Mason, P.J., Thomson, D.J., 1992. Stochastic backscatter in large-eddy simulations of boundary layers. J. Fluid Mech. 242 (28), 51–78.

Medici, D., Alfredsson, P., 2006. Measurements on a wind turbine wake: 3D effects and bluff body vortex shedding. Wind Energy: Int. J. Prog. Appl. Wind Power Convers. Technol. 9 (3), 219–236.

Medici, D., Alfredsson, P.H., 2008. Measurements behind model wind turbines: Further evidence of wake meandering. Wind Energy: Int. J. Prog. Appl. Wind Power Convers. Technol. 11 (2), 211–217.

Okulov, V.L., Sørensen, J.N., 2007. Stability of helical tip vortices in a rotor far wake. J. Fluid Mech. 576, 1–25.

Platis, A., Siedersleben, S.K., Bange, J., Lampert, A., Bärfuss, K., Hankers, R., Cañadillas, B., Foreman, R., Schulz-Stellenfleth, J., Djath, B., et al., 2018. First in situ evidence of wakes in the far field behind offshore wind farms. Sci. Rep. 8 (1), 1–10.

Porté-Agel, F., Meneveau, C., Parlange, M.B., 2000. A scale-dependent dynamic model for large-eddy simulation: Application to a neutral atmospheric boundary layer. J. Fluid Mech. 415, 261–284.

Posa, A., Broglia, R., 2021a. Characterization of the turbulent wake of an axial-flow hydrokinetic turbine via large-eddy simulation. Comput. & Fluids 216, 104815.

Posa, A., Broglia, R., 2021b. Momentum recovery downstream of an axial-flow hydrokinetic turbine. Renew. Energy 170, 1275–1291.

Posa, A., Broglia, R., 2022. Analysis of the momentum recovery in the wake of aligned axial-flow hydrokinetic turbines. Phys. Fluids 34 (10), 105130.

Posa, A., Broglia, R., Balaras, E., 2021. Instability of the tip vortices shed by an axial-flow turbine in uniform flow. J. Fluid Mech. 920, A19.

Posa, A., Broglia, R., Balaras, E., 2022. Recovery in the wake of in-line axial-flow rotors. Phys. Fluids 34 (4), 045104.

Pryor, S.C., Barthelmie, R.J., Shepherd, T.J., 2021. Wind power production from very large offshore wind farms. Joule 5 (10), 2663–2686.

Raibaudo, C., Piquet, T., Schliffke, B., Conan, B., Perret, L., 2022. POD analysis of the wake dynamics of an offshore floating wind turbine model. J. Phys.: Conf. Ser. 2265 (2), 022085.

Santoni, C., Carrasquillo, K., Arenas-Navarro, I., Leonardi, S., 2017. Effect of tower and nacelle on the flow past a wind turbine. Wind Energy 20 (12), 1927–1939.

Sarmast, S., Dadfar, R., Mikkelsen, R., Schlatter, P., Ivanell, S., Sørensen, J.N., Henningson, D., 2014. Mutual inductance instability of the tip vortices behind a wind turbine. J. Fluid Mech. 755, 705–731.

Schumann, U., 1975. Subgrid scale model for finite difference simulations of turbulent flows in plane channels and annuli. J. Comput. Phys. (4), 376–404.

Shaw, W.J., Berg, L.K., Debnath, M., Deskos, G., Draxl, C., Ghate, V.P., Hasager, C.B., Kotamarthi, R., Mirocha, J.D., Muradyan, P., Pringle, W.J., Turner, D.D., Wilczak, J.M., 2022. Scientific challenges to characterizing the wind resource in the marine atmospheric boundary layer. Wind Energy Sci. 7 (6), 2307–2334.

Singh, A., Howard, K.B., Guala, M., 2014. On the homogenization of turbulent flow structures in the wake of a model wind turbine. Phys. Fluids 26 (2), 025103.

Smagorinsky, J., 1963. General circulation experiments with the primitive equations: I. The basic experiment. Mon. Weather Rev. 91 (3), 99–164.

Sørensen, J.N., Shen, W.Z., 2002. Numerical modeling of wind turbine wakes. J. Fluids Eng. 124 (2), 393–399.

Stevens, R.J., Martínez-Tossas, L.A., Meneveau, C., 2018. Comparison of wind farm large eddy simulations using actuator disk and actuator line models with wind tunnel experiments. Renew. Energy 116, 470–478.

Sun, C., Tian, T., Zhu, X., Hua, O., Du, Z., 2021. Investigation of the near wake of a horizontal-axis wind turbine model by dynamic mode decomposition. Energy 227, 120418.

Troldborg, N., Sørensen, J.N., Mikkelsen, R., 2007. Actuator line simulation of wake of wind turbine operating in turbulent inflow. J. Phys.: Conf. Ser. 75 (1), 012063.

UK Government, 2020. Energy white paper. Powering our net zero future. URL https://www.gov.uk/government/publications/energy-white-paper-powering-our-net-zero-future.

Veers, P., Dykes, K., Lantz, E., Barth, S., Bottasso, C.L., Carlson, O., Clifton, A., Green, J., Green, P., Holttinen, H., Laird, D., Lehtomäki, V., Lundquist, J.K., Manwell, J., Marquis, M., Meneveau, C., Moriarty, P., Munduate, X., Muskulus, M., Naughton, J., Pao, L., Paquette, J., Peinke, J., Robertson, A., Rodrigo, J.S., Sempreviva, A.M., Smith, J.C., Tuohy, A., Wiser, R., 2019. Grand challenges in the science of wind energy. Science 366 (6464), eaau2027.

Vermeer, L., Sørensen, J.N., Crespo, A., 2003. Wind turbine wake aerodynamics. Prog. Aerosp. Sci. 39 (6–7), 467–510.

Widnall, S.E., 1972. The stability of a helical vortex filament. J. Fluid Mech. 54 (4), 641–663.

WindEurope, 2020. Offshore Wind in Europe: Key Trends and Statistics 2019. Tech. Rep., WindEurope.